


**Exciton diffusion in *h*BN-encapsulated monolayer MoSe<sub>2</sub>**Takato Hotta<sup>1</sup>, Shohei Higuchi<sup>1</sup>, Akihiro Ueda<sup>1</sup>, Keisuke Shinokita<sup>2</sup>, Yuhei Miyauchi<sup>2</sup>, Kazunari Matsuda<sup>2</sup>, Keiji Ueno<sup>3</sup>, Takashi Taniguchi<sup>4</sup>, Kenji Watanabe<sup>5</sup>, and Ryo Kitaura<sup>1,\*</sup><sup>1</sup>*Department of Chemistry, Nagoya University, Nagoya 464-8602, Japan*<sup>2</sup>*Institute of Advanced Energy, Kyoto University, Uji, Kyoto 611-0011, Japan*<sup>3</sup>*Department of Chemistry, Saitama University, Saitama 338-8570, Japan*<sup>4</sup>*International Center for Materials Nanoarchitectonics, National Institute for Materials Science, 1-1 Namiki, Tsukuba 305-0044, Japan*<sup>5</sup>*Research Center for Functional Materials, National Institute for Materials Science, 1-1 Namiki, Tsukuba 305-0044, Japan* (Received 1 May 2020; revised 16 August 2020; accepted 18 August 2020; published 21 September 2020)

Excitons, quasiparticles composed of an electron and a hole, play an important role in optical responses in low-dimensional nanostructures. In this work, we have investigated exciton diffusion in monolayer MoSe<sub>2</sub> encapsulated between flakes of hexagonal boron nitride (*h*BN/MoSe<sub>2</sub>/*h*BN). Through photoluminescence imaging and numerical solution of the two-dimensional diffusion equation, we revealed that temperature dependence of exciton mobility,  $\mu_{\text{ex}}$ , in *h*BN/MoSe<sub>2</sub>/*h*BN shows a nonsaturating increase at low temperature, which is qualitatively different from those of quantum wells composed of compound semiconductors. The ultraflat structure of monolayer MoSe<sub>2</sub> in *h*BN/MoSe<sub>2</sub>/*h*BN probably leads to the suppression of charged-impurity scattering and surface-roughness scattering.

DOI: [10.1103/PhysRevB.102.115424](https://doi.org/10.1103/PhysRevB.102.115424)**I. INTRODUCTION**

Excitons are quasiparticles composed of an electron and a hole. In response to optical excitations of semiconductors, electrons and holes are generated, leading to the formation of hydrogenlike bound states, called excitons, through Coulomb interaction. In a typical semiconductor such as silicon, the energy scale of binding energy between an electron and a hole is small (Si: 14.7 meV; room temperature: 25.8 meV), and in this case, the excitonic effect is not dominant in optical responses at room temperature [1]. At cryogenic temperature, however, the excitonic effect gives sharp resonances at energies lower than that of the band edge, drastically changing optical spectra.

In low-dimensional materials, the excitonic effect can dominate optical responses even at room temperature [2,3]. Due to the strong Coulomb interaction arising from the reduced dimension, exciton binding energy can reach several hundreds of meV in low-dimensional materials. For example, spectroscopic characterization and theoretical analyses have revealed that two-dimensional (2D) materials, including monolayer MoS<sub>2</sub>, WS<sub>2</sub>, and MoSe<sub>2</sub>, possess exciton binding energy of several hundreds of meV, which is much larger than that of the thermal energy at room temperature [4,5]. Due to this large binding energy, absorption and photoluminescence (PL) spectra of 2D materials are totally dominated by the excitonic effect, showing strong exciton resonances even at room temperature [6–10]. The excitonic effect is, thus, essential to understanding the optical properties of 2D materials.

In the optical response of 2D materials, exciton diffusion plays an important role. Because exciton binding energy is much larger than the thermal energy at room temperature, optical excitation inevitably leads to the formation of excitons in 2D materials. Due to the finite kinetic energy of generated excitons, excitons diffuse along a 2D plane before radiative or nonradiative recombination. The three processes, generation, diffusion, and recombination of excitons, always occur in response to optical excitations of 2D materials and, hence, it is crucial to understand exciton diffusion to understand the optical properties of 2D materials. In addition, understanding of exciton diffusion provides the basis to develop novel optoelectronics, excitonics, such as excitonic transistors, where control of the movement of excitons plays an essential role [11–14]. Although many works on excitons generation and recombination have been performed in the past 10 years, research focused on exciton diffusion is still sparse [15–20].

In this work, we have experimentally investigated the exciton diffusion in a 2D semiconductor, monolayer MoSe<sub>2</sub>. To suppress unwanted environmental effects arising from substrates and adsorbates, we encapsulated a monolayer MoSe<sub>2</sub> by flakes of hexagonal boron nitride (*h*BN). The *h*BN encapsulation yields ultraflat monolayer MoSe<sub>2</sub> that is separate from scattering sources in substrates [21,22]. PL spectra of *h*BN/MoSe<sub>2</sub>/*h*BN give intense peaks arising from radiative recombination of excitons, whereas peak intensity from trions is weak. PL imaging has clearly shown that excitons diffuse before recombination; bright regions in PL images are broader than corresponding laser spots used to excite samples. Detailed analyses based on solving the two-dimensional diffusion equation yielded that mobility of excitons increases as temperature decreases, revealing that scattering

\*r.kitaura@nagoya-u.jp

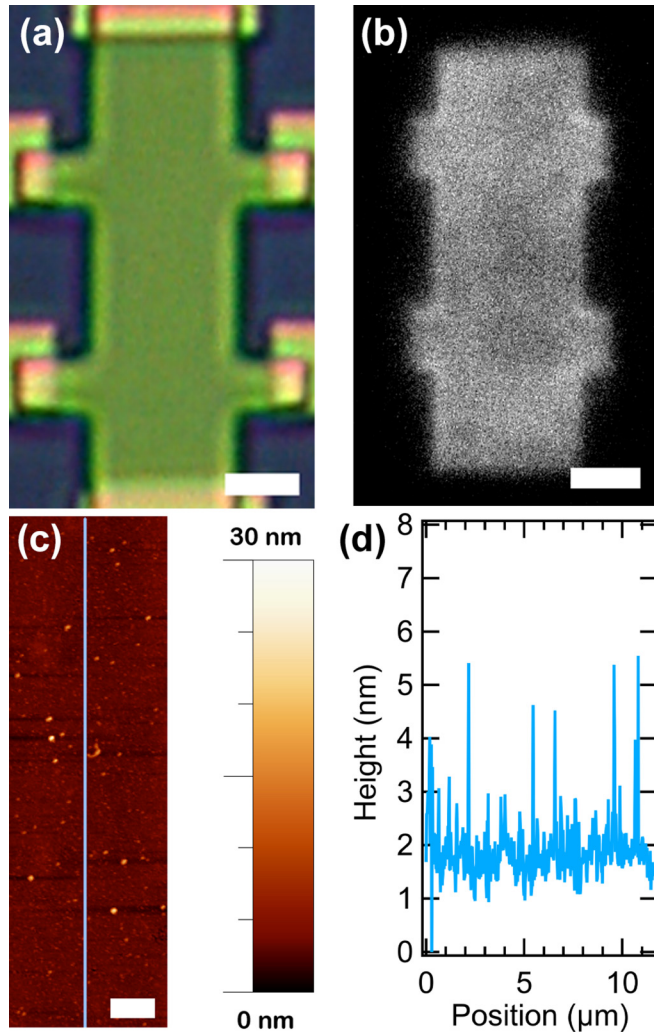


FIG. 1. (a) An optical microscope image of a *h*BN-encapsulated monolayer MoSe<sub>2</sub> fabrication. Details of the fabrication procedure are shown in the Supplemental Material [25]. Scale bar, 2  $\mu$ m. (b) A corresponding PL image. Scale bar, 2  $\mu$ m. (c), (d) An AFM image of the *h*BN-encapsulated monolayer MoSe<sub>2</sub> and a line profile along the line in the AFM image. Scale bar, 1  $\mu$ m.

is strongly suppressed in the *h*BN-encapsulated samples because of the ultraflat structure and charge neutrality of excitons.

## II. RESULTS AND DISCUSSION

### A. Fabrication and characteristics of *h*BN/MoSe<sub>2</sub>/*h*BN

We fabricated monolayer MoSe<sub>2</sub> sandwiched between *h*BN flakes, *h*BN/MoSe<sub>2</sub>/*h*BN, by the dry-transfer method; monolayer MoSe<sub>2</sub> exfoliated on SiO<sub>2</sub>/Si was picked up with a flake of *h*BN and transferred onto another flake of *h*BN [23–25]. Figure 1(a) shows an optical microscope image of the fabricated *h*BN/MoSe<sub>2</sub>/*h*BN. Green and blue contrasts correspond to *h*BN/MoSe<sub>2</sub>/*h*BN and a SiO<sub>2</sub>/Si substrate, respectively. The corresponding PL image measured at 300 K [Fig. 1(b)] gives uniform intensity all over the sample, indicating that there is no bubble or impurities encapsulated between *h*BN and MoSe<sub>2</sub>. Although there

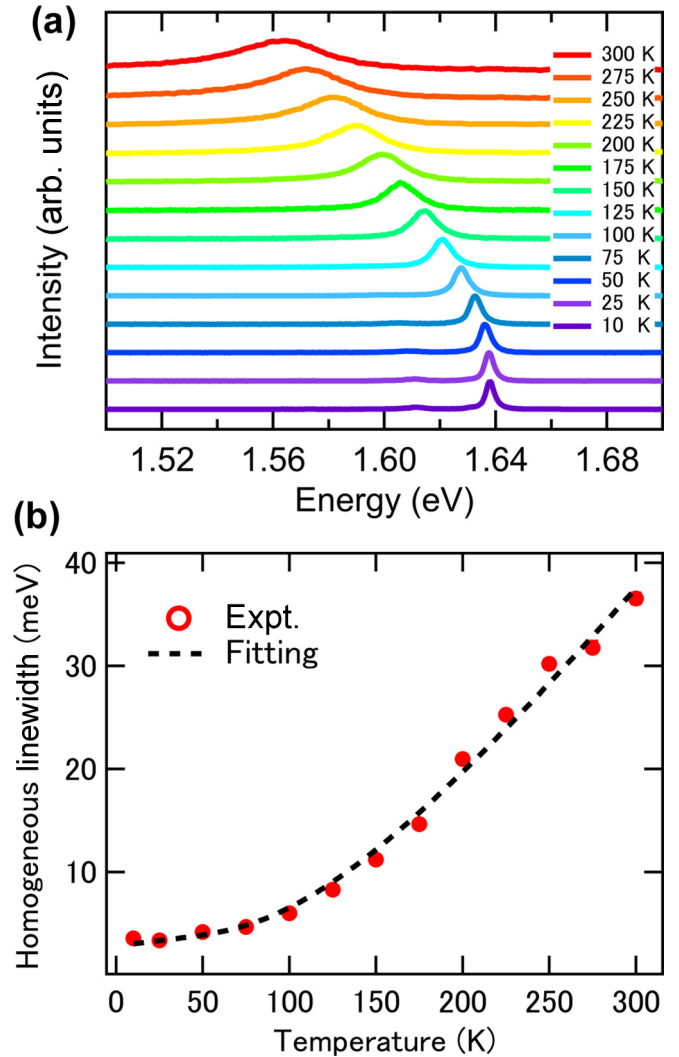


FIG. 2. Temperature dependence of PL spectra of a *h*BN-encapsulated monolayer MoSe<sub>2</sub>. The excitation wavelength of 550 nm with an excitation power density of 220 W cm<sup>-2</sup> was used for the measurements. (b) Temperature dependence of peak positions arising from radiative recombinations of excitons. The dotted line corresponds to the fitting with the equation shown in the main text.

are impurities that probably arise from impurities attached on the surface, there is no bubblelike structure observed in an AFM image of *h*BN/MoSe<sub>2</sub>/*h*BN [Figs. 1(c) and 1(d)], which is consistent with the uniform intensity observed in the PL image shown in Fig. 1(b). In this work, we used a relatively thick *h*BN flake, whose thickness is ca. 20 nm, to minimize the adverse substrate effect, which arises from charged impurities and surface roughness of SiO<sub>2</sub>/Si.

PL spectra measured at room temperature give a broad single peak, which originates from the radiative recombination of bright excitons, at room temperature. Figure 2(a) shows the temperature dependence of PL spectra of *h*BN/MoSe<sub>2</sub>/*h*BN. As seen in Fig. 2(a), the PL peak shifts toward the blue side as temperature decreases; this shift can be interpreted by the temperature-dependent change in the band gap of MoSe<sub>2</sub>; the temperature-dependent band-gap change has been well

reproduced by the equation based on phonon statistics [26], giving parameters of  $E_g = 1.68$  eV,  $a = 3.92 \times 10^{-2}$  eV, and  $b = 2.18 \times 10^2$  K (see Fig. S4 in the Supplemental Material [25], and [27–29]). The peak from radiative recombination of charged excitons (trions), which locates at energy 27 meV lower than that from excitons [30], is weak in this sample. This weak peak from trions means that unintentional carrier doping from the substrate and impurities is very small. Figure 2(b) shows the temperature dependence in a homogeneous linewidth (Lorentzian width), which was determined through peak fittings with the Voigt function; the Lorentzian linewidth was extracted whereas the Gaussian linewidth was fixed at the value determined at 10 K (1.2 meV); details on line-shape analyses are given in Fig. S3 [25]. As you can see, the linewidth values become narrower as temperature decreases. We have fitted the temperature dependence of homogeneous linewidths with the following equation, where the first, second, and third terms correspond to residual linewidth, acoustic phonon, and optical phonon scattering, respectively [31].

$$\gamma = \gamma_0 + c_1 T + \frac{c_2}{\exp\left(\frac{\Omega}{kT}\right) - 1}.$$

$\gamma_0$ ,  $c_1$ ,  $c_2$ ,  $\Omega$ ,  $k$ , and  $T$  in this equation represent residual linewidth, the constant for the acoustic phonon, the constant for the optical phonon, optical phonon energy, the Boltzmann constant, and temperature, respectively. The fitting yields the parameters of  $\gamma_0 = 2.8 \pm 0.5$  meV,  $c_1 = 20 \pm 3$   $\mu\text{eV K}^{-1}$ ,  $c_2 = 73 \pm 1$  meV, and  $\Omega = 32 \pm 3$  meV [32]. The contribution from the optical phonon is dominant at a temperature higher than about 100 K, and in the low-temperature region, the linewidth decreases linearly against temperature, which means acoustic phonon scattering is dominant at low temperature. The obtained values of  $\gamma_0$  and  $\Omega$  are consistent with values in the previous reports [33–35].

### B. Determination of diffusion coefficients

We have investigated exciton diffusion based on the PL imaging technique. Figures 3(a) and 3(b) show an image of the laser spot used to excite the sample and the corresponding PL image, respectively. We use a wavelength of 633 nm to excite the sample and a long-pass filter (650 nm) to filter out reflected light to form PL images. We have investigated excitation power dependence on PL intensity before the PL imaging measurements, and excitation power, which is well below the onset of exciton annihilation, was used for all measurements to avoid the formation of hot excitons [36,37]; details on the excitation power dependence on PL are given in Fig. S8 [25]. Note that the PL spectra measured with a low excitation power density of  $1.4 \text{ W cm}^{-2}$  show an intense peak arising from radiative recombination of  $K$ - $K$  direct excitons with negligible contribution from trions, biexcitons, and other types of exciton complexes, and in this case, two-body bound states,  $K$ - $K$  direct excitons, and their intervalley counterparts, dominate the diffusion processes. As seen in Figs. 3(a) and 3(b), the PL image is broader than the image of the laser spot. This broadening arises from the diffraction limit of light and exciton diffusion; excitons diffuse along the 2D plane before radiative recombination, leading to broadening of PL

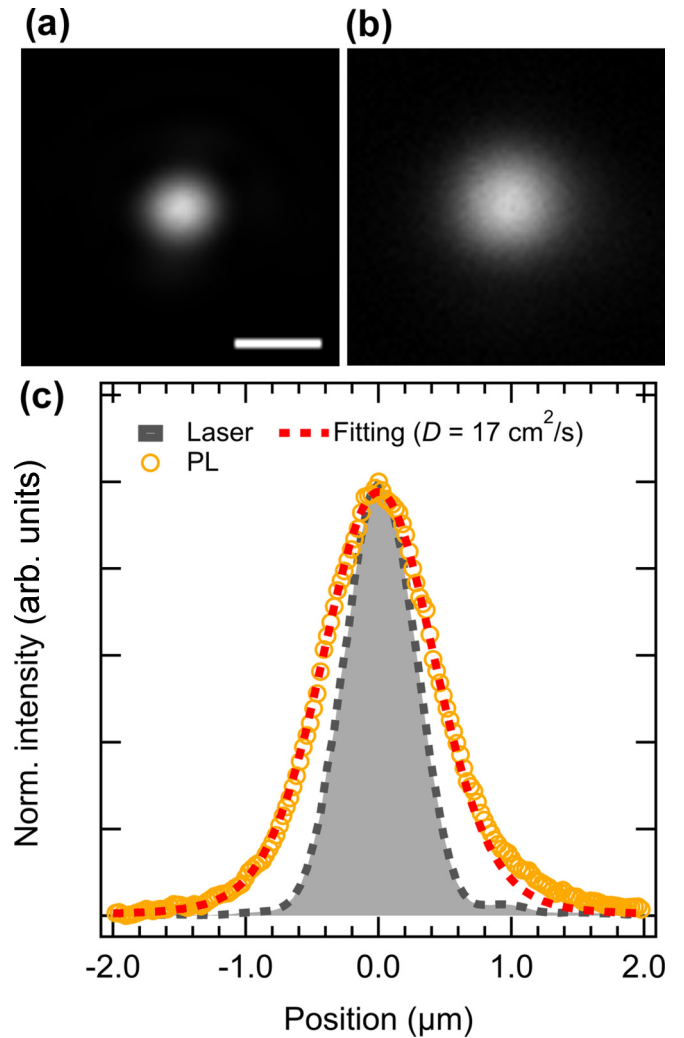


FIG. 3. (a), (b) An image of a laser spot used to excite of a laser spot used to excite the sample and the corresponding PL image measured at 20 K. Scale bar, 1  $\mu\text{m}$ . (c) A line profile of PL, the excitation laser spot, and the PL image shown in (a). A fitted curve based on solving the two-dimensional diffusion equation is also shown. These measurements were done with an excitation power density of  $1.4 \text{ W cm}^{-2}$ .

images. The diffraction limit of light can be modeled with the Gaussian-type point-spread function, whose Gaussian sigma,  $\sigma_{\text{diff}}$ , is  $0.21 \lambda/\text{NA}$  [38]; we use the center wavelength of exciton emission in PL,  $\lambda = 752.4\text{--}753.9$  nm and the value of numerical aperture ( $NA$ ) of 0.70 to evaluate the contribution from the diffraction limit. To evaluate the contribution of the exciton diffusion quantitatively, we have numerically solved the 2D diffusion equation with the exciton decay term.

$$\frac{\partial}{\partial t} N(x, y, t) = D \frac{\partial^2}{\partial x^2} N(x, y, t) + D \frac{\partial^2}{\partial y^2} N(x, y, t) - \frac{1}{\tau} N(x, y, t).$$

$x$ ,  $y$ , and  $t$  represent  $x$  and  $y$  coordinates in the 2D plane and time, respectively.  $N$ ,  $D$ , and  $\tau$  correspond to the number



of excitons, diffusion constant, and a lifetime of excitons. We assume that the diffusion of excitons is isotropic and the laser spot can be modeled as a Gaussian function. To solve the 2D diffusion equation, we need to know the exciton lifetime,  $\tau$ . We experimentally determined  $\tau$  through measurements of time-resolved PL intensity with the time-correlated single-photon counting (TCSPC) method. Note that the experimentally determined  $\tau$  corresponds to the effective lifetime of excitons, which results from both radiative and nonradiative decay of excitons. In most of the cases, time dependences of PL intensity are fitted with the two-component exponential decay model, where a long-lifetime component and a short-lifetime component simultaneously exist, whose origins are, perhaps, the  $K$ - $K$  direct excitons and the intervalley momentum- (spin-) forbidden dark excitons, respectively. We, therefore, have added up solutions of two independent diffusion equations with different lifetimes to take both the long-lifetime and the short-lifetime components into account. After solving the diffusion equations, we have summed obtained  $N(x, y)$  at different times (from zero to  $3\tau$ ) to calculate PL intensity distributions; we have convoluted the point-spread function to compare calculated PL intensity to the observed one. In Fig. 3(c), we show the line profile of a PL image measured at 20 K and the calculated PL profile. As shown in Fig. 3(c), the calculated PL profile reproduces the observed profile well, yielding the value of  $D$  of  $17 \text{ cm}^2 \text{ s}^{-1}$ . The diffusion constant can be converted to the mobility of excitons with the Einstein relation,  $\mu_{\text{ex}} = eD/k_B T$ , and the mobility at 20 K was determined to be  $9.8 \times 10^3 \text{ cm}^2 \text{ V}^{-1} \text{ s}^{-1}$ .

### C. Temperature dependence of exciton mobility

To have more insight on exciton diffusion in  $h\text{BN}/\text{MoSe}_2/h\text{BN}$ , we have measured the temperature dependence of exciton diffusion from 60 to 10 K. Using the measured  $\tau$  (Fig. S5 in the Supplemental Material [25]), we have performed the numerical solving of the diffusion equation at each temperature, yielding the temperature dependence of  $D$  and  $\mu_{\text{ex}}$  (Figs. 4 and S6 in the Supplemental Material [25]). As seen in the figures, while the obtained  $D$  are not susceptible to temperature, the  $\mu_{\text{ex}}$  increases as temperature decreases, and  $\mu_{\text{ex}}$  exceeds  $10^4 \text{ cm}^2 \text{ V}^{-1} \text{ s}^{-1}$  at low temperatures. A decrease in  $D$  is usually expected when temperature decreases due to the decrease in exciton thermal energy. In this case, however, the increase in  $\mu_{\text{ex}}$  cancels out the decrease of thermal energy, leading to the observed temperature dependence of  $D$ .

Let us compare the obtained results with those of GaAs-based quantum wells (QWs) [39,40]. In the case of QWs, it has been reported that  $\mu_{\text{ex}}$  increases as temperature decreases from room temperature to around 100 K, but as temperature decrease more,  $\mu_{\text{ex}}$  shows saturation and decreases as temperature goes down to cryogenic temperature. In the high-temperature region,  $\mu_{\text{ex}}$  increases as temperature decreases due to suppression of phonon scattering, and the same tendency is seen in  $h\text{BN}/\text{MoSe}_2/h\text{BN}$ . At cryogenic temperature, however, the difference between QWs and  $h\text{BN}/\text{MoSe}_2/h\text{BN}$  becomes obvious. The saturation and decrease in  $\mu_{\text{ex}}$  in QWs arise from the interface roughness

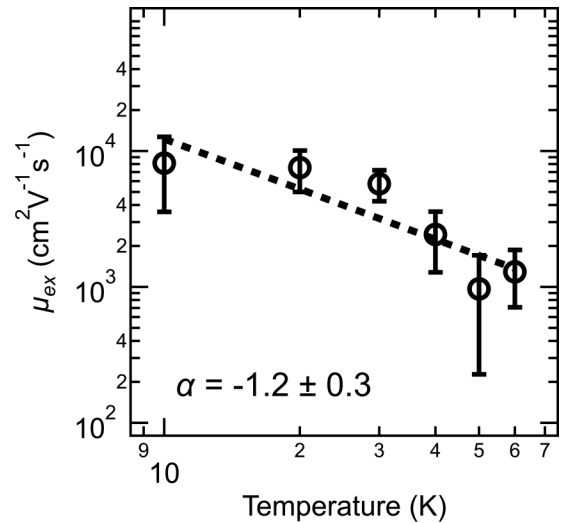


FIG. 4. Temperature dependence of exciton mobility,  $\mu_{\text{ex}}$ . The dotted line is a fitted line with the equation of  $\ln(\mu_{\text{ex}}) = \ln(T^\alpha)$ , where  $\alpha$  is  $-1.2 \pm 0.3$  as shown in the figure.

scattering, which dominates the scattering process at low temperature; the interface roughness scattering is prominent in the case of thin QWs. In contrast, despite the ultrathin structure of monolayer  $\text{MoSe}_2$ , whose thickness is about 0.7 nm,  $\mu_{\text{ex}}$  in  $h\text{BN}/\text{MoSe}_2/h\text{BN}$  shows a nonsaturating increase throughout the temperature range investigated, 10–60 K. This nonsaturating increase should originate from the atomically flat structure of  $\text{MoSe}_2$  in  $h\text{BN}/\text{MoSe}_2/h\text{BN}$ , where the atomically flat  $h\text{BN}$  flakes ensure the flatness of  $\text{MoSe}_2$ . The atomically flat structure in  $h\text{BN}/\text{MoSe}_2/h\text{BN}$  significantly suppresses the interfacial roughness scattering, leading to the nonsaturating  $\mu_{\text{ex}}$ . QWs and 2D materials are similar systems in terms of 2D electronic systems, but the ultrathin and ultraflat structure of 2D materials gives a distinctly different nature to excitons in 2D materials.

Because excitons are neutral objects, scattering from charged impurities should be suppressed in the case of excitons. Previous studies on carrier transport of  $h\text{BN}$ -encapsulated TMDs have revealed that carrier mobility is enhanced in the case of the multilayer structure. For example, Cui *et al.* have reported that six-layer  $\text{MoS}_2$  shows carrier mobility of  $3 \times 10^4 \text{ cm}^2 \text{ V}^{-1} \text{ s}^{-1}$  whereas monolayer  $\text{MoS}_2$  shows  $\sim 10^3 \text{ cm}^2 \text{ V}^{-1} \text{ s}^{-1}$  at low temperature [21]. They have concluded that the significant difference in mobility arises from interfacial impurity scattering; the thicker the  $\text{MoS}_2$  is, the larger the distance between the interfacial impurity and the carriers is. This clearly demonstrates that charged-impurity scattering is one of the dominant limiting factors of carrier mobility in TMDs. In contrast, in the case of excitons, charged-impurity scattering should be suppressed due to the charge neutrality of excitons, and this might play an essential role in the observed large  $\mu_{\text{ex}}$ . Note that the absolute value of  $\mu_{\text{ex}}$  depends strongly on the exciton lifetime, and the determination of precise values of  $\mu_{\text{ex}}$  needs further measurement with a sample whose lifetime is long enough to minimize experimental error. However, lower bound estimation of  $\mu_{\text{ex}}$  with the upper bound value of exciton lifetimes still ranges on

the order of  $\sim 10^3 \text{ cm}^2 \text{ V}^{-1} \text{ s}^{-1}$ , which should result from the suppression of interfacial impurity scattering.

Suppression of charged-impurity scattering can be seen in the temperature dependence of the linewidth of the excitonic PL peak. As discussed above, at low temperature ( $< 100 \text{ K}$ ), the linewidth of the excitonic peak decreases linearly against temperature, which means that acoustic phonon scattering is the dominant factor in this temperature regime. This is consistent with the observed temperature dependence in  $\mu_{\text{ex}}$ . A least-square fitting of the observed temperature dependence of  $\mu_{\text{ex}}$  in Fig. 4 gives the relation of  $\mu_{\text{ex}}(T) \propto T^\alpha$  ( $\alpha = -1.2 \pm 0.3$ ). It is well known that carrier mobility limited by acoustic phonon scattering is proportional to  $T^{-1}$  in 2D electronic systems; this relation is close to the observed relation,  $\mu_{\text{ex}}(T) \propto T^{-1.2}$ . A similar  $\mu$ - $T$  relation is also seen in the other  $h\text{BN}/\text{MoSe}_2/h\text{BN}$  sample (Fig. S7 [25]), and this strongly suggests that impurity scattering is suppressed in exciton diffusion in a high-quality  $h\text{BN}/\text{MoSe}_2/h\text{BN}$  sample investigated in this study.

### III. CONCLUSION

In conclusion, we have investigated exciton diffusion in  $h\text{BN}/\text{MoSe}_2/h\text{BN}$  through PL imaging and numerical solution of the 2D diffusion equation. Images of laser spots used to excite the sample are smaller than those of corresponding PL images, which means that the generated excitons

diffuse along the 2D plane before radiative and nonradiative recombination. Detailed analyses based on numerically solving the 2D diffusion equation have yielded exciton mobility,  $\mu_{\text{ex}}$ , at temperatures from 10 to 60 K. The observed temperature dependence of  $\mu_{\text{ex}}$  shows a nonsaturating increase at low temperature, which is significantly different from those of QWs. The ultraflat structure of monolayer  $\text{MoSe}_2$  in  $h\text{BN}/\text{MoSe}_2/h\text{BN}$  probably leads to the suppression of charged-impurity scattering and surface-roughness scattering, and the observed temperature dependence of linewidths is consistent with the suppression of scatterings. Our work shows the exciton diffusion characteristic of ultraflat 2D semiconductors, which provides a basis to understand basic optical responses in 2D semiconductors.

### ACKNOWLEDGMENTS

This work was supported by JSPS KAKENHI Grants No. 20H5664, No. JP20H02566, No. JP19F19368, No. JP16H06331, No. JP16H03825, No. JP16H00963, No. JP15K13283, No. JP25107002, and No. JP19J15359; and JST CREST Grants No. JPMJCR16F3 and No. JPMJCR19H4. K.W. and T.T. acknowledge support from the Elemental Strategy Initiative conducted by the MEXT, Japan, Grant No. JPMXP0112101001; JSPS KAKENHI Grant No. JP20H00354; and the CREST (JPMJCR15F3), JST.

- 
- [1] K. L. Shaklee and R. E. Nahory, *Phys. Rev. Lett.* **24**, 942 (1970).  
 [2] G. Wang, A. Chernikov, M. M. Glazov, T. F. Heinz, X. Marie, T. Amand, and B. Urbaszek, *Rev. Mod. Phys.* **90**, 021001 (2018).  
 [3] T. Mueller and E. Malic, *npj 2D Mater. Appl.* **2**, 29 (2018).  
 [4] M. M. Ugeda, A. J. Bradley, S. F. Shi, F. H. da Jornada, Y. Zhang, D. Y. Qiu, W. Ruan, S. K. Mo, Z. Hussain, Z. X. Shen, F. Wang, S. G. Louie, and M. F. Crommie, *Nat. Mater.* **13**, 1091 (2014).  
 [5] B. Zhu, X. Chen, and X. Cui, *Sci. Rep.* **5**, 9218 (2015).  
 [6] M. Okada, A. Kutana, Y. Kureishi, Y. Kobayashi, Y. Saito, T. Saito, K. Watanabe, T. Taniguchi, S. Gupta, Y. Miyata, B. I. Yakobson, H. Shinohara, and R. Kitaura, *ACS Nano* **12**, 2498 (2018).  
 [7] M. Okada, Y. Miyauchi, K. Matsuda, T. Taniguchi, K. Watanabe, H. Shinohara, and R. Kitaura, *Sci. Rep.* **7**, 322 (2017).  
 [8] D. Kozawa, R. Kumar, A. Carvalho, K. Kumar Amara, W. Zhao, S. Wang, M. Toh, R. Ribeiro, A. Castro Neto, K. Matsuda, and G. Eda, *Nat. Commun.* **5**, 4543 (2014).  
 [9] A. Arora, M. Koperski, K. Nogajewski, J. Marcus, C. Faugeras, and M. Potemski, *Nanoscale* **7**, 10421 (2015).  
 [10] A. Arora, K. Nogajewski, M. Molas, M. Koperski, and M. Potemski, *Nanoscale* **7**, 20769 (2015).  
 [11] D. Unuchek, A. Ciarrocchi, A. Avsar, K. Watanabe, T. Taniguchi, and A. Kis, *Nature* **560**, 340 (2018).  
 [12] K. F. Mak and J. Shan, *Nat. Photonics* **10**, 216 (2016).  
 [13] Q. Wang, K. Kalantar-Zadeh, A. Kis, J. Coleman, and M. Strano, *Nat. Nanotechnol.* **7**, 699 (2012).  
 [14] B. Baugher, H. Churchill, Y. Yang, and P. Jarillo-Herrero, *Nat. Nanotechnol.* **9**, 262 (2014).  
 [15] M. Kulig, J. Zipfel, P. Nagler, S. Blanter, C. Schuller, T. Korn, N. Paradiso, M. M. Glazov, and A. Chernikov, *Phys. Rev. Lett.* **120**, 207401 (2018).  
 [16] T. Kato and T. Kaneko, *ACS Nano* **10**, 9687 (2016).  
 [17] F. Cadiz, C. Robert, E. Courtade, M. Manca, L. Martinelli, T. Taniguchi, K. Watanabe, T. Amand, A. C. H. Rowe, D. Paget, B. Urbaszek, and X. Marie, *Appl. Phys. Lett.* **112**, 152106 (2018).  
 [18] N. Kumar, Q. N. Cui, F. Ceballos, D. W. He, Y. S. Wang, and H. Zhao, *Nanoscale* **6**, 4915 (2014).  
 [19] J.-W. Kang, J.-W. Jung, T. Lee, J. G. Kim, and C.-H. Cho, *Phys. Rev. B* **100**, 205304 (2019).  
 [20] J. Wang, Y. Guo, Y. Huang, H. Luo, X. Zhou, C. Gu, and B. Liu, *Appl. Phys. Lett.* **115**, 131902 (2019).  
 [21] X. Cui, G. H. Lee, Y. D. Kim, G. Arefe, P. Y. Huang, C. H. Lee, D. A. Chenet, X. Zhang, L. Wang, F. Ye, F. Pizzocchero, B. S. Jessen, K. Watanabe, T. Taniguchi, D. A. Muller, T. Low, P. Kim, and J. Hone, *Nat. Nanotechnol.* **10**, 534 (2015).  
 [22] L. Wang, I. Meric, P. Y. Huang, Q. Gao, Y. Gao, H. Tran, T. Taniguchi, K. Watanabe, L. M. Campos, D. A. Muller, J. Guo, P. Kim, J. Hone, K. L. Shepard, and C. R. Dean, *Science* **342**, 614 (2013).  
 [23] Y. Hoshi, T. Kuroda, M. Okada, R. Moriya, S. Masubuchi, K. Watanabe, T. Taniguchi, R. Kitaura, and T. Machida, *Phys. Rev. B* **95**, 241403(R) (2017).  
 [24] Y. Uchiyama, A. Kutana, K. Watanabe, T. Taniguchi, K. Kojima, T. Endo, Y. Miyata, H. Shinohara, and R. Kitaura, *npj 2D Mater. Appl.* **3**, 1 (2019).  
 [25] See Supplemental Material at <http://link.aps.org/supplemental/10.1103/PhysRevB.102.115424> for details of fabrication of

- h*BN-encapsulated MoSe<sub>2</sub> flake; PL measurements and fitting PL peaks by Voigt function; least-square fittings with Lorentzian and Gaussian functions; temperature dependence of peak positions; time-resolved PL; solving 2D diffusion equation and fitting of the PL profile,  $\tau$ ;  $D$  and  $\mu_{\text{ex}}$  in the other sample; excitation power density dependence of PL intensity.
- [26] L. Viña, S. Logothetidis, and M. Cardona, *Phys. Rev. B* **30**, 1979 (1984).
- [27] S. Helmrich, R. Schneider, A. Achtstein, A. Arora, B. Herzog, S. de Vasconcellos, M. Kolarczik, O. Schöps, R. Bratschitsch, U. Woggon, and N. Owschimikow, *2D Mater.* **5**, 045007 (2018).
- [28] H. Li, X. Zhu, Z. Tang, and X. Zhang, *J. Lumin.* **199**, 210 (2018).
- [29] J. Huang, T. B. Hoang, and M. H. Mikkelsen, *Sci. Rep.* **6**, 22414 (2016).
- [30] G. Shepard, J. Ardelean, O. Ajayi, D. Rhodes, X. Zhu, J. Hone, and S. Strauf, *ACS Nano* **11**, 11550 (2017).
- [31] S. Rudin, T. L. Reinecke, and S. Segall, *Phys. Rev. B* **52**, 11517 (1995).
- [32] Note: The errors of parameters ( $\gamma_0$ ,  $c_1$ ,  $c_2$ , and  $\Omega$ ) were obtained as parameter errors in a least-square fitting analysis. The determined parameters have two significant figures, and more accurate determination needs additional data points.
- [33] S. Shree, M. Semina, C. Robert, B. Han, T. Amand, A. Balocchi, M. Manca, E. Courtade, X. Marie, T. Taniguchi, K. Watanabe, M. M. Glazov, and B. Urbaszek, *Phys. Rev. B* **98**, 035302 (2018).
- [34] A. Molina-Sánchez and L. Wirtz, *Phys. Rev. B* **84**, 155413 (2011).
- [35] G. Gupta and K. Majumdar, *Phys. Rev. B* **99**, 085412 (2019).
- [36] D. F. Cordovilla Leon, Z. Li, S. W. Jang, and P. B. Deotare, *Phys. Rev. B* **100**, 241401(R) (2019).
- [37] R. Perea-Causín, S. Brem, R. Rosati, R. Jago, M. Kulig, J. Ziegler, J. Zipfel, A. Chernikov, and E. Malic, *Nano Lett.* **19**, 7317 (2019).
- [38] B. Zhang, J. Zerubia, and J. C. Olivo-Marin, *Appl. Opt.* **46**, 1819 (2007).
- [39] H. Hillmer, A. Forchel, S. Hansmann, M. Morohashi, E. Lopez, H. P. Meier, and K. Ploog, *Phys. Rev. B* **39**, 10901 (1989).
- [40] D. Oberhauser, K. H. Pantke, J. M. Hvam, G. Weimann, and C. Klingshirn, *Phys. Rev. B* **47**, 6827 (1993).